

# Fatigue and Damage Tolerance Analysis of a Hybrid Composite Tapered Flexbeam

American Helicopter Society Forum  
May 9-11, 2001 in Washington DC.

Gretchen B. Murri  
Research Engineer  
Army Vehicle Technology Directorate, Hampton, VA  
g.b.murri@larc.nasa.gov

Jeffrey R. Schaff  
Research Engineer/Scientist  
United Technologies Research Center  
East Hartford, CT  
schaffjr@utrc.utc.com

Alan L. Dobyns  
Senior Structures Specialist  
Sikorsky Aircraft, Stratford, CT  
ADobyns@SIKORSKY.COM

## ABSTRACT

The behavior of nonlinear tapered composite flexbeams under combined axial tension and cyclic bending loading was studied using coupon test specimens and finite element (FE) analyses. The flexbeams used a hybrid material system of graphite/epoxy and glass/epoxy and had internal dropped plies, dropped in an overlapping stepwise pattern. Two material configurations, differing only in the use of glass or graphite plies in the continuous plies near the midplane, were studied. Test specimens were cut from a full-size helicopter tail-rotor flexbeam and were tested in a hydraulic load frame under combined constant axial-tension load and transverse cyclic bending loads. The first delamination damage observed in the specimens

occurred at the area around the tip of the outermost ply-drop group in the tapered region of the flexbeam, near the thick end. Delaminations grew slowly and stably, toward the thick end of the flexbeam, at the interfaces above and below the dropped-ply region. A 2D finite element model of the flexbeam was developed. The model was analyzed using a geometrically non-linear analysis with both the ANSYS and ABAQUS FE codes. The global responses of each analysis agreed well with the test results. The ANSYS model was used to calculate strain energy release rates (G) for delaminations initiating at two different ply-ending locations. The results showed that delaminations were more inclined to grow at the locations where they were observed in the test specimens. Both ANSYS and ABAQUS were used to calculate G values associated with delamination initiating at the observed location but growing in different interfaces, either above or below the ply-ending group toward the thick end, or toward the thin end from the tip of the resin pocket. The different analysis codes generated the same trends and comparable peak values, within 5-11% for each delamination path. Both codes showed that delamination toward the thick region was largely mode II, and toward the thin region was predominantly mode I. The calculated peak G-values from either analysis predict delamination is most likely to occur along the same interface where it was observed in the test specimens. Calculated peak G values were used with material characterization data to calculate a curve relating the fatigue life of the specimens, N, to the applied transverse load, V, for a given constant axial load.

## NOMENCLATURE

$b$	delamination length along taper above ply ending, mm
$b/l$	delamination length along taper below ply ending, mm
$a$	delamination length toward thin region, mm
$E_1, E_2$	Young's moduli in 1- and 2- directions, GPa
$G$	total strain energy release rate, J/m <sup>2</sup>
$G_{12}$	shear moduli, GPa

---

*Presented at the American Helicopter Society 57th Annual Forum, Washington, DC, May 9-11, 2001. Copyright © 2001 by the American Helicopter Society International, Inc. All rights reserved.*

$G_I$	mode I strain energy release rate, $J/m^2$
$G_{II}$	mode II strain energy release rate, $J/m^2$
$N$	number of loading cycles
$P$	axial tension load, kN
$V$	measured transverse (bending) load, kN
$t_{ply}$	ply thickness in PATRAN model
$v$	transverse displacement at tip of flexbeam, mm
$\theta$	flexbeam flapping angle, degrees
$\delta$	transverse stroke of ATB test machine, mm
$\epsilon$	flexbeam surface strain, $\mu\epsilon$
$\epsilon_{max}$	maximum cyclic surface strain, $\mu\epsilon$
$\nu_{12}$	Poisson's ratio

## INTRODUCTION

Polymeric composites are used extensively in the manufacture of dynamic structural components within the rotorcraft industry. One application is hingeless, bearingless composite helicopter rotor hubs, which have reduced weight and drag, as well as fewer parts, compared to metal hubs. However, unlike metals, there are no fracture mechanics based methods for predicting strength and life of these structures considering damage. An analysis and test methodology that incorporates damage, mechanics, and failure probability is critical to demonstrate reliability and forecast maintenance issues. Currently, the damage tolerance of rotorcraft composite structures is verified through testing. The state-of-the-art models used to simulate damage are interlaminar fracture methods based on energy-release-rate and virtual crack closure principles, as proposed by O'Brien in ref. 1 and summarized by Martin in ref. 2. The prediction of onset-of-delamination under tension-bending cyclic loading was demonstrated by Murri and O'Brien in ref. 3 for a helicopter flexbeam sub-element.

During flight, the helicopter rotor hub arm experiences axial tension loading due to the centrifugal forces (CF), as well as bending loads in the flapping flexure region. In order to accommodate this bending, the stiffness of the flapping flexure region is changed by varying the thickness of the hub arm. This thickness change is accomplished by

terminating internal plies at multiple locations along the length of the flexbeam. However, these internal ply-drop locations create discontinuities, at which delaminations may initiate [3-8]. Many parameters, such as the material properties, taper geometry, lay-up orientation, and ply-drop pattern of the flexbeam, can affect the flexbeam's susceptibility to delamination under the combined loading. In refs. 4-17, delamination failure in tapered laminates with internal ply drops under pure tension loads was studied. References 4-6, 9, 13, and 14 considered tapered laminates of a variety of different materials and with different internal ply-drop configurations. In each study, it was determined that delamination onset occurred at the ply-drops, as a result of high interlaminar stresses at those locations. In ref. 18, the effect of combined tension and bending loading on a tapered laminate with a linear or nonlinear taper geometry was studied. A simple finite element (FE) model was developed using beam elements, which were able to account for the effect of membrane loads on the flexural response of the laminate. The predicted surface strains from the FE analyses agreed well with measured results from simple coupon specimens with either linear or nonlinear tapers.

In ref. 3, the effect of combined tension-bending loading on glass-epoxy laminates with a nonlinear taper was studied. The nonlinear taper was created by terminating internal plies at various locations along the length, in a non-uniform staggered ply-drop scheme. A 2D finite element (FE) model of this flexbeam was developed and axial tension and cyclic bending loading was modeled. Coupon specimens of the same material, lay-up, and geometry were tested under tension-bending loading. Delamination was simulated in the model to duplicate the observed delaminations from the experiments. At each increment of delamination growth, the strain energy release rate,  $G$ , was calculated. The calculated  $G$  values were used with material characterization data to calculate fatigue lives of the flexbeams. The calculated values agreed very well with the measured fatigue lives of the test specimens.

In this study, a representative section of a hybrid graphite/glass tail rotor flexbeam was selected as a

benchmark structure for analysis and testing. A series of flexbeam sub-element specimens were cut from a full-size flexbeam and were subjected to axial tension and cyclic flatwise-bending loading. A 2D finite element model that truly represents the same geometry, lay-up and hybrid material system as the tested specimens was developed. The model was analyzed using the ANSYS and ABAQUS FE codes, using geometric nonlinear options and incorporating contact effects. The analyses were used to calculate strain energy release rates for modeled delamination growth at several interfaces. Results of the analyses were compared to each other and to the test results.

## EXPERIMENTS

### Specimen Geometry and Test Conditions

The flexbeam is the primary load-bearing member of the rotor assembly and transfers bending and torsion loads from the blade to the rotor. Flexbeams are therefore designed to provide high edgewise rigidity for stability, and low torsional and flatwise rigidity for flexibility. To accommodate this flexibility requirement, the flexbeam thickness varies along the length, with a thin center region of unidirectional plies, a taper region where unidirectional and off-axis plies are added in steps along the length, and a thick attachment region of unidirectional and off-axis plies.

Laboratory testing was performed on sub-element size specimens cut from the outboard taper region of full size flexbeams on a commercial Sikorsky tail rotor. Figure 1 shows a typical test specimen. The specimens had a nonlinear taper design and the lay-up was symmetric about the midplane. The specimen thickness varied from 129 plies at the thick end, to 39 plies at the thin end. The layup consists of 0, 45 and -45 degree plies, with the continuous plies being strictly 0-degree and the ply-ending groups being either 45/-45 pairs, or [0<sub>2</sub>/45/-45] groups. The specimens were fabricated using a combination of S2/8552 glass/epoxy and graphite/epoxy. Material properties and nominal ply thickness for both materials are given in Table 1.

Table 1. Typical laminae room temperature material properties.

Material	graphite/epoxy	glass/epoxy S2/8552
E <sub>1t</sub> , GPa (msi)	161.35 (23.40)	47.58 (6.90)
E <sub>2t</sub> , GPa (msi)	11.38 (1.65)	13.10 (1.90)
E <sub>1c</sub> , GPa (msi)	143.4 (20.80)	46.88 (6.80)
E <sub>2c</sub> , GPa (msi)	12.75 (1.85)	17.93 (2.60)
G <sub>12</sub> , GPa (msi)	5.17 (0.75)	5.03 (0.73)
ν <sub>12</sub>	0.32	0.27
Thickness, mm (in)	0.152 (0.006)	0.152 (0.006)

Two different flexbeam configurations were studied. They were identical in exterior taper geometry and material systems, but the lay-ups differed in the use of either graphite plies or glass plies closest to the mid-plane. The different lay-ups will be referred to in this report as graphite-midplane specimen (GRMS) or glass-midplane specimen (GLMS), respectively. The lengths of the GRMS and GLMS specimens are 203.2 mm (8-inch) and 165.1 mm (6.5-inch), respectively. The gage length was shortened from the original 203.2 mm to 165.1 mm to reduce the transverse stroke required to achieve the desired strain levels, and to improve the ATB performance. For the two gage lengths, only the length of the thin region varied; the length of the tapered region was always 80.7 mm (3.17 in.). The thick region was the same length for both specimen types, and was completely within the bottom grip for all specimens. The nominal dimensions of the GLMS specimens are shown in fig. 2.

Figure 3 shows a photograph of the tapered region of a GLMS specimen at the specimen edge. The figure shows the hybrid materials, as well as the continuous belt-ply groups and the dropped-ply group. The tapered section is divided into three regions, each containing 4 to 7 ply-ending packs. Within each of these packs, 2 to 4 plies are terminated in stepwise fashion. The terminated plies (ply-endings) are identified by region number, pack number, and ply-ending number. Pack numbers and ply-ending numbers increase, moving from the flexbeam upper and lower surfaces toward the midplane. Ply-endings 111 and 311 are defined in

fig 3. As the sketch in fig. 3 shows, the terminated plies are dropped in an overlapping pattern, so that the plies closest to the midplane are shortest and are terminated first.

#### Axial Tension Bending Machine

The flexbeam specimens were tested in a servo-hydraulic load frame, called the Axial-Tension Bending (ATB) machine, which is shown schematically in fig. 4. The ATB can be used to produce constant axial tension loading, combined with cyclic bending loading. As fig. 4 shows, the axial load cell is located above the top grip, but below the pivot connecting the axial and transverse actuators. Therefore, the axial tension load,  $P$ , "rotates" with the specimen as the transverse load is applied and remains constant as the specimen flexes under the transverse bending load,  $V$ . With the axial tension load applied under load control, and the transverse bending applied using stroke control, a constant membrane load should be maintained throughout the loading cycle.

#### Static Tests

Before testing, specimens were instrumented with strain gages along the length on the left and right sides of the flexbeam as shown in fig. 2, with gages in both the thin and tapered regions. Using the end of the taper region at the thick end as a reference (STA 32.84 shown on fig. 2), the specimens were inserted into the lower grip with the thick end completely in the fixed bottom grip, and the bottom of the tapered region (STA 32.84) flush with the top of the lower grip. The gage length between the grips was either 203.2 mm (8 inches) for the GRMS specimen or 165.1 mm (6.5 inches) for the GLMS specimens.

Static testing was conducted on all specimens, prior to fatigue testing, to determine the relationship between applied loads and specimen deflection and surface strains. These relationships were used to determine axial load and cyclic transverse displacements for fatigue testing. For static excursions, a constant axial tension load,  $P$ , was applied and held constant, while the transverse stroke,  $\delta$ , was applied, in steps of approximately 2.54 mm (0.1 inch), up to a maximum stroke of 45.7 mm

(1.8 inch). At each transverse stroke step, the strains as referenced in fig. 2 were recorded, as well as the transverse flexbeam tip-displacement,  $v$ , and flapping angle,  $\theta$ . The flexbeam tip-displacement was measured using a spring-loaded direct-current displacement transducer (DCDT) which was mounted to the side of the load frame and detected the displacement of a bracket attached to the centerline of the top grip. The flapping angle was measured by means of a digital protractor mounted to the top grip. Figure 5 shows a schematic of the specimen in the ATB with loads and deflections labeled. Observation of specimen markings and load-displacement measurements indicated no evidence of slipping.

#### Fatigue Tests

For fatigue testing, the tension load and transverse displacement for each specimen were chosen based on a desired maximum surface strain level, rather than a prescribed transverse deflection or flapping angle. The axial tension load was chosen as the load that resulted in a strain of approximately  $2500 \mu\epsilon$  in the constant thickness region of the specimen approximately 74 mm from upper grip, i.e., gages 5 and 7a in fig. 2. Then, with the axial load applied, a transverse displacement was chosen to correspond to a desired maximum strain level at the beginning of the tapered region, ply ending 111; i.e., gage 4 or 4a of fig. 2. This region is chosen for comparison with baseline fullscale flexbeam data, which references strains at this location. The maximum strain levels for fatigue testing were between  $5628 \mu\epsilon$  and  $8000 \mu\epsilon$ . A minimum transverse displacement was chosen to give an R-ratio ( $\epsilon_{min}/\epsilon_{max}$ ) of approximately  $R=0.1$  at gage 4 for each test. Asymmetric loading was used in this study, rather than fully-reversed ( $R=-1$ ) to more accurately simulate the actually loading experienced by a flexbeam in flight, and for better comparison with material characterization data from fatigue 4ENF tests at  $R=-0.1$ .

Prior to fatigue tests, the specimen edges were painted with a thin coating of white paint, which is brittle and makes delaminations easier to see. The axial load was applied first, at a loading rate of 2.22 kN/sec (500 lb./sec). Then the transverse stroke was applied to achieve the mean transverse

displacement. The transverse stroke was then applied sinusoidally, at a frequency of 3 Hz.

During the fatigue testing, the axial and transverse loads were briefly monitored to verify the repeatability and accuracy of the loads chosen from the static excursions. A representative axial and transverse load-time history is plotted in fig. 6, at  $N=24732$  cycles into the test, for a prescribed axial tension load of 35.14 kN (7900 lbs.). Good repeatability of the loading by the Teststar controller (2%) was observed. However, fig. 6 indicates the axial load is not held constant as the cyclic transverse load is applied. Rather, the axial load varies by about  $\pm 21\%$ , from 27.76 kN (6240 lbs.) to 42.70 kN (9600 lbs.). The actual fatigue loads were recorded and used in subsequent analysis.

## ANALYSIS

### Finite Element Model

A brief summary of the finite element model is provided. The model was developed to duplicate the nonlinear tapered geometry of the flexbeam and the boundary conditions of the loading apparatus. The model, generated using the PATRAN (v8.0) modeling software and shown in fig. 7, was 2D and was symmetric about the midplane. Individual plies were modeled such that the two outermost ply-ending packs from each region of fig. 3 were discretely created, using square elements and one element per ply. The location of the ply-endings was determined from design drawings, and the resin pocket size at the end of terminated plies was estimated based on average values from photomicrograph inspection. In contrast, the plies near the centerline and below the outermost ply endings are coarsely modeled, using three layers of elements and merging plies in the material definition. Figure 8 shows a close-up of the finite element representation of ply-ending 111.

The model was analyzed using both the ANSYS and ABAQUS FE packages. A two-dimensional eight-noded plane-strain quadrilateral element was used in both analyses. ANSYS and ABAQUS differ in their implementation of element coordinate systems, orthotropic materials, constraint equations, and solution algorithms. A representative ply-ending

problem was solved by both FE codes and calculated strain energy release rates agreed within 2%. For combined tension-bending loading, a nonlinear solution was used with stress stiffening and large deformation options in both codes. Three-dimensional orthotropic properties, i.e., x-z plane, were determined based on the unidirectional elastic constants given in Table 1, using laminated plate theory to calculate smeared properties in the coarsely meshed regions. In order to assign the correct material properties to the elements in the tapered region, a local coordinate system was assigned to each element in the model, with the element 1-direction parallel to the element side from the local node  $i$  to local node  $i+1$ , as shown in fig. 8. The local t-n coordinate system was then used to define the material properties of each element.

For both analyses, fixed conditions were simulated at the thick end of the model. For the ANSYS model, beam elements, with  $EI=1.74E8$  N-m<sup>2</sup> ( $6.05E8$  lb-in<sup>2</sup>), were used to simulate the ATB loading fixture and upper grip, extending 172 mm (6.75 in.) beyond the flexbeam tip, as shown in fig. 5. The axial and transverse forces were applied at the tip of the beam model. For the ABAQUS analysis, the upper grip and loading fixture are represented by rectangular elements with a cross-section equal to the thin end of the composite flexbeam. Those elements representing the loading fixture were assigned moduli to yield a bending stiffness,  $EI$ , equivalent to the actual ATB fixtures. The axial tension load was then applied to the free end of the model as a distributed load and the transverse bending was applied as a prescribed displacement in the negative-y direction.

The manner in which the resin pocket is modeled ahead of the ply-ending was an important detail in model development. Figure 9 shows a micrograph of the area around a ply-drop. To represent the resin pocket, a right triangular region was meshed. Figure 9 shows that the thickness of the ply increases ahead of the resin pocket as the ply ending is introduced. Hard nodal points were created at ply-ending and resin pocket regions to create a mesh that accounted for the reduced fiber volume region ahead of the ply-ending, while maintaining a smooth continuous slope

with the surface of the flexbeam. The size of the resin pocket was estimated from photomicrograph observations. The length of the resin zone in the FE model and in the specimens varied from  $11t_{ply}$  at ply-ending 111, to  $3.3t_{ply}$  at ply-ending 314. Typically the resin pocket length for the first ply-ending in a given ply-pack was larger than downstream ply-endings. The ply-ending geometry was characterized for 12 specimens and significant variability was noted. For example, the mean and standard deviation for ply-ending 311 was measured as  $6.07 t_{ply}$  and  $2.20 t_{ply}$ , respectively.

#### Strain Energy Release Rate Computation

In order to simulate a crack or delamination in the flexbeam, multi-point constraint (MPC) nodes were incorporated in the model at the interfaces around ply-endings 111 and 311. Delaminations were then simulated at those interfaces by incrementally releasing the MPCs.

The Virtual Crack Closure Technique (VCCT) was used to calculate strain energy release rates at each step of simulated delamination growth. The VCCT calculates the mode I (opening) and mode II (sliding shear) components of strain energy release rate ( $G_I$  and  $G_{II}$ , respectively), using the forces at the delamination tip, and the relative displacements behind the delamination tip. Figure 10 shows the equations for  $G_I$  and  $G_{II}$ ; as well as the forces at nodes  $i$  and  $j$ ; and the displacements at nodes  $l$  and  $m$ , all in the  $n$ - $t$  coordinate system. These nodal forces and displacements were obtained from the ABAQUS and ANSYS output files. Because these flexbeams experience large deflections, the displacements and forces must be measured in the local coordinate system; i.e., the normal-tangential ( $n$ - $t$ ) coordinate system for the deformed elements (see fig. 10). Details of these calculations are given in refs. 19 and 20. The total strain energy release rate,  $G$ , is obtained by summing the individual mode components. Hence,

$$G = G_I + G_{II}$$

since  $G_{III}=0$  for plane strain conditions.

#### Mesh Refinement Study

A convergence study was performed using ANSYS to determine the effect of the number of elements per modeled ply in the region of the delamination tip, on the calculated strain energy release rate,  $G$ . A representative section of the finite element model of the flexbeam was extracted for study. Four mesh densities were considered in this study: 1 element/ply, 2 element/ply, 4 element/ply, and 8 element/ply.

A brief summary of the finite element model used for the mesh refinement study is provided. A reduced model section, representing the first two ply endings (111 and 112) of the outboard taper region between STA 28.393 to STA 30.024 of fig 2, was taken from the full FE model. The model was fixed at STA 30.024 and constraint equations were applied at STA 28.393 to enforce a rigid plane at the specimen tip. The axial and transverse forces were applied at the tip and distributed by mass node and constraint equations;  $F_x=-4.54$  kN (-1020 lbs.),  $F_y=-0.489$  kN (-110 lbs.). For the combined axial and transverse load case, a non-linear solution was executed with stress stiffening and large deformation activated.

First, a model with 1 element/ply was analyzed for several delamination lengths, where the crack started from the resin tip and extended along the path toward the 'thin' end of the flexbeam.  $G_I$  and  $G_{II}$  were calculated as a function of delamination length,  $a$ . From this result a delamination length of  $a=8t_{ply}$  was selected for the convergence study. The results are shown in fig. 11 for  $G_I$  and  $G_{II}$  versus the number of elements used per ply, at constant  $a=8t_{ply}$ . This length was selected since  $G_I$  and  $G_{II}$  are nearly equal in magnitude at  $a=8t_{ply}$ , thus the refinement study is inclusive of both modes. As the figure shows, increasing the number of elements from one per ply to eight per ply causes a change in  $G_I$  and  $G_{II}$  of 4.7%. These results indicate that a mesh of 1 element/ply was adequate for the analysis using 2D higher-order elements.

## RESULTS

#### Global Response

Combined tension-bending fatigue testing was performed on three specimens: a 203.2 mm (8-inch)

long GRMS, and two 165.1 mm (6.5 inch) long GLMS specimens (GLMS1 and GLMS2). Surface strains in the FE model were calculated using both the ABAQUS and ANSYS analyses and were compared to measured values from the static testing to determine how accurately the model reproduced the global behavior of the test specimens. Figure 12 shows the measured and predicted transverse displacement,  $v$ , of the GRMS specimen tip for a prescribed fixed axial load and varying transverse load,  $V$ , from the ANSYS and ABAQUS analyses. Overall, the global response of the specimen and ATB fixture is well predicted by the FE result.

Figure 13 shows the strain comparisons along the length of the flexbeam for GRMS specimen. Measured and calculated results are shown at an axial load of 42.7 kN (9610 lbs.) and a transverse displacement of -60.7 mm (-2.39 inches). As the figure shows, the ANSYS and ABAQUS results are almost identical, and are in good agreement with the measured strains for both the tension and compression surfaces of the flexbeam. The maximum surface strains occurred in the thinner region of the taper, at approximately 53 mm from the bottom grip, near gages 3 and 3a in fig. 2. Similarly, fig. 14 shows equally good results for the tension surface of the GLMS1 specimen. Based on these results, the FE models appear to duplicate the global response of the specimens under loading in the ATB very well.

#### Fatigue Tests

The specimens were visually monitored periodically for delamination onset and growth throughout the fatigue loading cycle. Both the left and right edges were monitored. In all three tested specimens, the initial damage occurred on the “tension” side of the specimen, in the tapered region. The location of the initial damage site along the length was the same for all the specimens, and suggested that the delamination had started at ply-ending 311. For all the specimens, the damage was visible on both edges of the specimen, (left and right), at the same location, and had the same general appearance, indicating that uniform length delaminations had formed across the width of the

specimen. Once the initial damage formed, the delaminations always tended to grow toward the thick end of the laminate. In all cases the delamination growth was very slow and stable. Very little delamination growth was observed to grow from the initiation site toward the thin end of the flexbeam (see fig. 16).

The GRMS specimen was fatigue tested with a constant axial load of 42.52 kN (9560 lbs.) and cyclic transverse load from -8.76 kN to 1.638 kN (-1970 lbs. to 368 lbs.). This corresponded to maximum and minimum surface strains at gage 2 of 8000 and 1010  $\mu\epsilon$ , respectively, with an R-ratio of 0.126. The specimen was inspected at N=2900 cycles and damage was already visible on the “tension” side of the specimen, in the area near ply ending 311. At first the delamination was evident on the one edge only. As the fatigue loading continued, damage became evident at the corresponding location on the other edge also, and delaminations could be observed growing toward the thick end of the flexbeam. By N=28,855 cycles, delaminations existed at the interfaces above and below ply-ending 311, and had grown almost all the way to the bottom grip. Figure 15 shows the specimen after N=43,900 cycles. Along with the initial delamination surfaces, several more delaminations had formed at neighboring interfaces between the original interfaces and the midplane. These delaminations appeared to have started at ply-ending locations 321 and 331. Fatigue testing was continued to N=281,000 cycles, at which point there was extensive delamination damage in the tapered region on both edges, but no unstable delamination growth or catastrophic failure. Figure 16 shows a photomicrograph of the area around ply-ending 311. Inspection of the photomicrograph suggests that the damage began as a tension crack behind the resin pocket. The likely delamination interfaces are labeled in fig. 16 as the interface under 311 (labeled interface *b*), the interface above 311 (interface *b*), or the interface forward from the tip of the resin pocket toward the thin region of the flexbeam (interface *a*). Results for the GRMS specimen indicate a preference for growth along interface *b*, based on experimental observation

and delamination length compared to interfaces *a* and *b*.

The GLMS1 specimen was fatigue tested under a constant axial load of 35.14 kN (7900 lbs.) and cyclic transverse load between -5.68kN and 2.15 kN (-1277 lbs. to 483 lbs). This corresponded to maximum and minimum surface strains at gage 2 of 6859 and 673  $\mu\epsilon$ , respectively ( $R=0.098$ ). The fatigue test resulted in delamination initiation on the left and right edges of the specimen at 22,000 cycles and 27,686 cycles, respectively. The initial damage occurred at the same location along the length as for the GRMS specimen. As the fatigue testing was continued, delaminations grew from this damage site, toward the thick end of the flexbeam. Figure 17 shows photographs of the delamination damage at three different values of *N*. As the photos show, delaminations were much more inclined to grow along interfaces *b* and *b'*, than along interface *a*, similar to the GRMS specimen, although there is a small amount of detectable growth along *a* visible at  $N=55,880$  and at  $N=119,300$ .

The GLMS2 specimen was fatigue tested under slightly less severe conditions than GLMS1, at a constant axial load of 31.58 kN (7100 lbs.) and cyclic transverse load between -4.45 kN and 1.63 kN (-1000 lbs. to 367 lbs.). Those load levels resulted in maximum and minimum surface strains at gage 2 of 5628 and 684  $\mu\epsilon$ , respectively ( $R=0.121$ ). For this specimen, delamination could not be detected visually until approximately  $N=330,00$  cycles. At that point, a tension crack at the resin pocket at ply-ending 311 was faintly visible. By  $N=340,000$  cycles, delaminations were obvious along interfaces *b* and *b'*. These delaminations grew slowly with continued loading. Figure 18 shows photos of the front face at  $N=486,00$  cycles and at  $N>500,000$  cycles. Unlike specimens GRMS and GLMS1, delaminations did not form at any other interfaces.

### Strain Energy Release Rate Analysis

In this work, the strain energy release rate (SERR) analysis had three purposes: quantify likely location of delamination at a ply-ending group, identify the expected delamination path, and predict the onset of delamination. To accomplish the first goal,

comparisons of preliminary ANSYS SERR results at two ply-ending locations were made, to identify the critical location. Then detailed SERR analyses were performed using both the ANSYS and ABAQUS models for delaminations originating at the critical location, and growing along multiple delamination paths. In all cases, a resin crack was simulated at the ply-ending by uncoupling the nodes along the desired path. The tension crack that formed behind the resin pocket was modeled by using separate uncoupled nodes at the midside node location on the adjoining elements at that location (see fig. 16).

The ANSYS GRMS model was used to obtain strain energy release rates for delaminations initiating from both ply-endings 111 and 311 and growing along paths *a*, *b*, and *b'*, for loading conditions  $P=42.52$  kN (9560 lbs.) and  $V=-8.76$  kN (-1970 lbs.) and modeling the tension crack open behind the resin pocket. Figure 19 shows  $G_I$  and  $G_{II}$  results for ply ending 111 along paths *a*, *b*, and *b'*. In this analysis, the peak value,  $73 \text{ J/m}^2$  ( $0.417 \text{ in-lb/in}^2$ ), corresponds to  $G_I$  along path *a* at ply-ending 111 at length  $a=2t_{\text{ply}}$ . Figure 20 shows the ANSYS results at ply-ending 311. The  $G_{II}$ -value for delamination along *b'* reaches a peak of  $964 \text{ J/m}^2$  ( $5.50 \text{ in-lb/in}^2$ ) at  $a=2t_{\text{ply}}$ , then reaches a second peak as the delamination approaches the second ply-ending, 312. For delaminations along interface *b*, a peak value of  $G_{II}$  is reached at the same delamination length as the *b'* interface. As fig. 20 shows, delamination growth along either *b* or *b'* is primarily mode II for this analysis. The *G*-values for delamination along *a* are very small compared to the other interfaces, and are primarily mode I.

The ABAQUS analysis was also used to calculate  $G_I$ ,  $G_{II}$ , and mode ratio for delaminations growing along *a*, *b*, and *b'* in the GRMS model. Individual components of energy release rate and mode ratio results are presented in fig. 21 and 22 for completeness. The mode percentages, plotted in fig. 22 as  $G_{II}/G_{\text{total}}$ , also follow the same trend as the ANSYS model, with growth along *b* and *b'* predominantly mode II, and along *a* predominantly mode I. A quantitative comparison of ABAQUS and ANSYS SERR solutions is provided later for critical fracture modes and paths. A study of the SERR

results of both models suggests that based on the magnitude of  $G_{II}$ , the critical ply-ending location is 311. This was confirmed in the experiments, since no delaminations formed at location 111 for any specimen for the full duration of testing. The analysis also showed that, of the three paths modeled, delamination is most likely to occur along interface  $bl$ . Strain energy release rate values along interface  $a$  were very small compared to those along  $b$  and  $bl$ , suggesting that delamination growth in that direction is less likely. Both these trends were observed in the test specimens. The results from these analyses indicate that for a delamination initiating at location 311, delaminations are most likely to grow along interface  $bl$ .

Figures 23-25 compare the ERR results from ANSYS and ABAQUS for the dominant mode for interfaces  $a$ ,  $b$ , and  $bl$ , respectively. For delamination along  $a$ , fig. 23 shows good agreement of the magnitude and shape of the  $G_I$  curves within 5%. Similarly good agreement of both  $G_{II}$  solutions is shown in fig. 24 for the  $b$  interface. Figure 25 compares the  $G_{II}$  results for a delamination along  $bl$ . The trends of the two curves are similar and the first peak is well matched. However, the values at the second peak location are reasonable, i.e., within 11%. The labels at the top of fig. 25 show the changing nature of the interface where delamination  $bl$  grows (i. e., between two graphite plies, or between resin and a ply). As the curves show, as a resin pocket is encountered, G-values decrease; then they increase again as the delamination approaches a new ply-ending, reaching a peak, and then decreasing as the delamination tip approaches another resin pocket.

The trends observed in this study are similar to those observed in ref. 3, for a different nonlinear tapered flexbeam, where the terminated plies were dropped in a non-uniform staggered manner, and the ply-ending was modeled as a group with smeared properties, rather than as individual dropped plies. In that study, delaminations grew first toward the thick end of the laminate, at the interfaces above and below the ply-ending group. The results from the FE model in ref. 3 showed that delamination toward the

thick end was largely mode II, and toward the thin region was primarily mode I.

#### Fatigue Life Prediction

In ref. 3, peak values of calculated strain energy release rate were used with measured G vs. N data from material characterization tests of the modeled material to calculate a curve relating delamination onset and the number of loading cycles. A similar approach was used here to generate a curve of the applied load, V, as a function of the number of cycles to delamination onset. Figure 26 shows results of static and cyclic 4ENF (mode II) tests on graphite/epoxy [22]. Because the delamination growth along  $bl$  is at least 95% mode II near the peak value, it was considered acceptable to use the mode II data for an initial attempt. A power curve was fit through the data, with the equation

$$G_{II\max}=1307.7N^{-0.16463}$$

Then it was assumed that delamination would initiate in the test specimens when the peak G-value from the FE analysis equaled the cyclic  $G_{II\max}$  at which delamination started in the 4ENF tests. That is,

$$\left[ \frac{G_{FE}}{V_{FE}^2} \right] = \frac{G_{II\max}}{V^2}$$

where the terms on the left are the peak G for delamination along  $bl$ , and the applied maximum transverse cyclic bending load,  $V_{FE}$ , from the FE model. The terms on the right are the  $G_{II\max}$  curve from the 4ENF tests and V is the applied maximum transverse cyclic load in the fatigue test. Substituting the equation for  $G_{II\max}$ , the peak value of  $G_{FE}$  (964 J/m<sup>2</sup>), and the load  $V_{FE}$  from the model (8.76 kN), and solving for the load V, results in the curve shown in fig. 27, relating the number of loading cycles, N, to the applied transverse load, given a constant axial load of P=42.52 kN (9560 lbs). Also plotted in fig. 27 is the number of cycles to failure of the GRMS specimen. The calculated fatigue life is somewhat lower than the observed life of the specimen. However, the curve fit to the 4ENF data was done using only 3 static test points and 3 fatigue points, all at similar values of N, that were 1 to 2 orders of magnitude greater than the test data point. Also, the

peak value of  $G$  was calculated to occur at a delamination length of 2 ply-thicknesses ( $2t_{ply}$ ). However, the mesh reduction study was done using a delamination length of  $8t_{ply}$ . It is not known whether a finer mesh in peak- $G$  area would change the calculated  $G$ -values there. It is important also to realize that this life prediction methodology calculates the cycles to the onset of delamination growth once the tension crack has formed behind the resin pocket, but does not account for the number of cycles necessary to open the tension crack. A life prediction methodology that could also account for the cycles to open the resin crack would result in more accurate life predictions, especially for tests of short duration, such as the example discussed in fig. 27.

Several issues need to be considered in evaluating this fatigue life prediction methodology for these flexbeams. More 4ENF data points are necessary to achieve a more accurate  $G$  vs.  $N$  curve. Also, another mesh reduction study is necessary in the area around the calculated peak  $G$  values. Additionally, more fatigue data from flexbeam testing is necessary for comparison with calculated fatigue lives. The number of cycles to open the resin crack where delaminations growth starts should be accounted for in the life prediction, as this may be a significant part of the total life, especially for short duration tests. These concerns will be dealt with in future work, where the above procedure will be repeated using FE results from the GLMS model and comparing with a larger number of test results.

## CONCLUSIONS

Nonlinear tapered flexbeam laminates were cut from a full-size composite helicopter rotor hub flexbeam and were tested under combined constant axial tension and cyclic bending loads. Two configurations were studied. They both used a hybrid graphite/glass material system, but differed in the use of graphite or glass plies near the midplane. The terminated plies were dropped in an overlapping stepwise pattern. All of the specimens failed by delaminations first starting around the tip of the outermost ply-drop group in the tapered region, and growing toward the thick region of the flexbeam. As

the cyclic loading was continued, delaminations continued to grow at those interfaces, until the delaminations extended to the base of the flexbeam. Delaminations also grew along the same direction at adjacent ply-ending interfaces. At all ply-ending locations there was significantly less delamination growth into the thin region of the flexbeam.

A 2D finite element model was developed which closely approximated the flexbeam geometry, boundary conditions, and loading. The model was analyzed using two geometrically nonlinear FE codes, ANSYS and ABAQUS. Both analysis codes showed that the FE model was able to accurately replicate the global response and measured surface strains of the coupon specimens under the combined loading. Delaminations of various lengths were simulated in the model by releasing multipoint constraints (MPC) and defining contact elements. Strain energy release rates ( $G$ ) were calculated using the virtual crack closure technique (VCCT). The ANSYS code was used to calculate strain energy release rates for delaminations starting at two different ply-ending locations in the model, and growing at each of three interfaces. Those results clearly showed that delaminations were more likely to grow at ply-ending interface 311, in good agreement with experimental observations. Both ANSYS and ABAQUS were used to calculate strain energy release rates for delaminations initiating at that ply-ending location, and growing along three possible delamination paths. The peak calculated  $G$  values were used with material characterization data to calculate fatigue life curves, for comparison with test data. The following results were determined:

- (1) Delaminations originated at the tip of the outermost ply-ending group and showed a strong preference to grow at the interfaces above and below the ply-ending, toward the thick end of the flexbeam, rather than toward the thin region of the flexbeam.
- (2) Delamination growth was slow and stable for both specimen types. As the initial delaminations grew close to the bottom grip, multiple delaminations could appear at parallel interfaces, on both faces of the flexbeams.

- (3) Calculated G-values for delamination growth along 3 different interfaces using the ANSYS and ABAQUS FE codes indicated the same trends and relatively good agreement of magnitude, 5-11%.
- (4) Both analyses indicated that delamination should be more likely to grow along the interface below the ply-ending, toward the thick end of the flexbeam.
- (5) Calculation of the mode ratios from both analyses for the different modeled delaminations showed that delamination growth toward the thick region was mostly Mode II, whereas delamination growth in the opposite direction was predominantly Mode I.
- (6) A curve relating applied transverse load V and loading cycles to delamination onset was calculated using cyclic  $G_{I\max}$  data from 4ENF tests and calculated peak G values. The observed failure point of the GRMS test specimen occurred later than the V vs. N curve predicted. A mesh refinement study at the delamination length where the peak G-value occurred may result in a different calculated peak G. Additional flexbeam test data are necessary to adequately evaluate this fatigue life prediction method.

#### ACKNOWLEDGMENT

Technical tasks described in this document include tasks supported with shared funding by the U.S. rotorcraft industry and the Government under the RITA/NASA cooperative agreement number 0076, Advanced Rotorcraft Technology, August 16, 1995.

#### REFERENCES

- (1) O'Brien, T. K., "Towards a Damage Tolerance Philosophy for Composite Materials and Structures," *Composite Materials: Testing and Design, Vol. 9, ASTM STP 1059*, S. P. Garbo, Ed., American Society for Testing and Materials, Philadelphia, 1990, pp. 7-33.
- (2) Martin, R. H., "Incorporating Interlaminar Fracture Mechanics into Design," International Conference on Designing Cost- Effective Composites, ImechE Conference Transactions, London, Sep. 15-16, 1998, pp. 83-92.
- (3) Murri, G. B., O'Brien, T. K., and Rousseau, C. Q., "Fatigue Life Methodology for Tapered Composite Flexbeam Laminates," *Journal of the American Helicopter Society*, Vol. 43, No. 2, April 1998, pp. 146-155.
- (4) Fish, J. C. and Lee, S. W., "Tensile Strength of Tapered Composite Structures," AIAA Paper No. 88-2252, *Proceedings of the 30th AIAA/ASME/ASCE/AHS Structures, Structural Dynamics and Materials (SDM) Conference*, Williamsburg, VA, April 1988, pp. 324-333.
- (5) Hoa, S. V., Daoust, J., and Du, B. L., "Interlaminar Stresses in Tapered Laminates," *Polymer Composites*, Vol. 9, No. 5, October 1988, pp. 337-344.
- (6) Llanos, A. S., Lee, S. W., and Vizzini, A. J., "Delamination Prevention in Tapered Composite Structures under Uniaxial Tensile Loads," AIAA Paper No. 90-1063, *Proceedings of the 31st AIAA/ASME/ASCE/AHS Structures, Structural Dynamics and Materials (SDM) Conference*, Long Beach, CA, April 1990, pp. 1242-1252.
- (7) Murri, G. B., Salpekar, S. A., and O'Brien, T. K., "Fatigue Delamination Onset Prediction in Unidirectional Tapered Laminates," *Composite Materials: Fatigue and Fracture (Third Volume)*, ASTM STP 1110, T. K. O'Brien, Ed., American Society for Testing and Materials, Philadelphia, 1991, pp. 312-339.
- (8) Wisnom, M. R., "Delamination in Tapered Unidirectional Glass Fibre-Epoxy Under Static Tension Loading," AIAA Paper No. 91-1142, *Proceedings of the 32nd AIAA/ASME/ASCE/AHS Structures, Structural Dynamics and Materials (SDM) Conference (Part 2)*, Baltimore, MD, April 1991, pp. 1162-1172.
- (9) Daoust, J. and Hoa, S. V., "Parameters Affecting Interlaminar Stresses in Tapered Laminates

- Under Static Loading Conditions," *Polymer Composites*, Vol. 10, No. 5, October 1989, pp. 374-383.
- (10) Trethewey, B. R., Jr; Gillespie, J. W., Jr; and Wilkins, D. J., "Interlaminar Performance of Tapered Composite Laminates," *Proceedings of the American Society for Composites, 5th Technical Conference*, East Lansing, MI, June 1990, pp. 361-372.
- (11) Botting, A. D., Vizzini, A. J., and Lee, S. W., "The Effect of Ply-Drop Configuration on the Delamination Strength of Tapered Composite Structures," *Proceedings of the AIAA/AHS/ASME/ASCE/ASC 33rd Structures, Structural Dynamics and Materials Conference*, Dallas, TX, Apr. 1992, pp. 40-47.
- (12) Fish, J. C. and Vizzini, A. J., "Delamination of Ply-Drop Configurations," *Composite Materials: Testing and Design (Eleventh Volume)*, ASTM STP 1206, E. T. Camponeshi, Jr., Ed., American Society for Testing and Materials, Philadelphia, 1993, pp. 323-332.
- (13) Kemp, B. L. and Johnson, E. R., "Response and Failure Analysis of a Graphite-Epoxy Laminate Containing Terminating Internal Plies," AIAA Paper No. 85-0608, *Proceedings of the 26th AIAA/ASME/ASCE/AHS Structures, Structural Dynamics and Materials (SDM) Conference*, Orlando, FL, April 1985, pp. 13-24.
- (14) Curry, J. M., Johnson, E. R., and Starnes, J. H., "Effect of Dropped Plies on the Strength of Graphite-Epoxy Laminates," *Proceedings of the 29th AIAA/ASME/ASCE/-9AHS Structures, Structural Dynamics and Materials (SDM) Conference*, Monterey, CA, April 1987, pp. 737-747.
- (15) Armanios, E. A. and Parnas, L., "Delamination Analysis of Tapered Laminated Composites Under Tensile Loading," *Composite Materials: Fatigue and Fracture (Third Volume)*, ASTM STP 1110, T. K. O'Brien, Ed., American Society for Testing and Materials, Philadelphia, 1991, pp. 340-358.
- (16) Salpekar, S. A., Raju, I. S., and O'Brien, T. K., "Strain Energy Release Rate Analysis of Delamination in a Tapered Laminate Subjected to Tension Load," *Proceedings of the American Society for Composites, Third Technical Conference*, Seattle, WA, Sept. 1988, pp. 642-654.
- (17) Murri, G. B., O'Brien, T. K., and Salpekar, S. A., "Tension Fatigue of Glass/Epoxy and Graphite/Epoxy Tapered Laminates," *Journal of the American Helicopter Society*, Vol. 38, No. 1, Jan. 1993, pp. 29-37.
- (18) O'Brien, T. K., Murri, G. B., Hagemeyer, R., and Rogers, C., "Combined Tension and Bending Testing of Tapered Composite Laminates," *Applied Composite Materials*, Vol. 1, No. 6, 1995, pp. 401-413.
- (19) Rybicki, E. F., and Kanninen, M. F., "A Finite Element Calculation of Stress-Intensity Factors by a Modified Crack-Closure Integral," *Engineering Fracture Mechanics*, Vol. 9, 1977, pp. 931-938.
- (20) Raju, I. S., "Simple Formulas for Strain-Energy Release Rates with Higher Order and Singular Finite Elements," NASA Contractor Report 178186, December 1986.
- (21) Krueger, R., Minguet, P. J., and O'Brien, T. K., "A Method for Calculating Strain Energy Release Rates in Preliminary Design of Composite Skin/Stringer Debonding Under Multiaxial Loading," *Composite Structures: Theory and Practice*, ASTM STP 1383, P. Grant and C. Q. Rousseau, Eds., American Society for Testing and Materials, West Conshohocken, PA, 2000, pp. 105-128.
- (22) Hansen, P., and Martin, R., "DCB, 4ENF, and MMB Delamination Characterisation of S2/8552 and IM7/8552," Materials Engineering Research Laboratory Ltd. (MERL), Hertford, U.K., N68171-98-M-5177, 1999.



Figure 1. Hybrid tapered flexbeam test specimen.

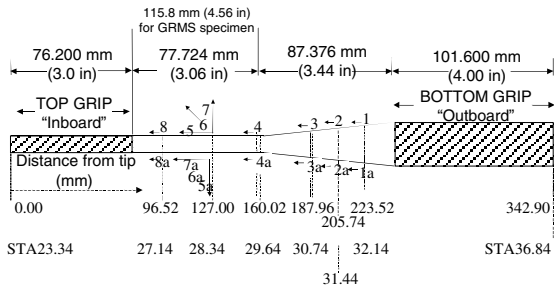


Figure 2. Schematic of glass midplane specimen (GLMS) with net dimensions and strain gages.

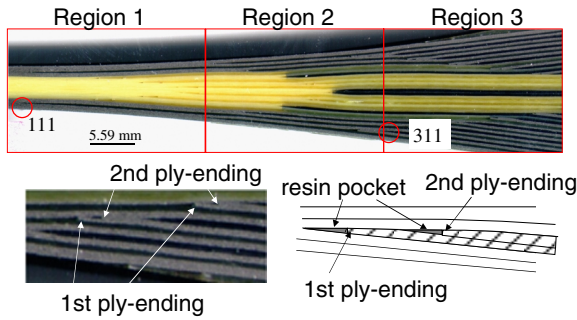


Figure 3. Photograph of edge of hybrid composite flexbeam with internal ply-drops.

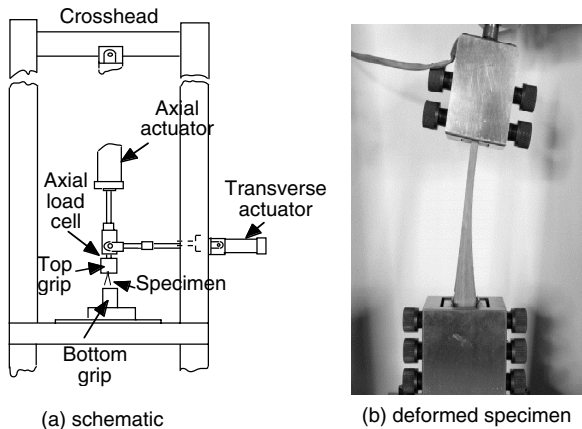


Figure 4. Axial tension and bending test stand (ATB) and deformed flexbeam specimen.

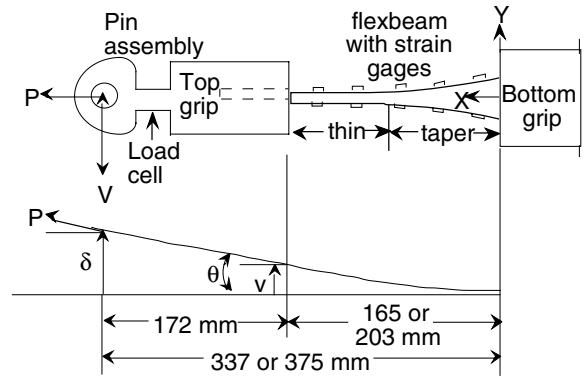


Figure 5. Schematic of test specimen and loading fixtures with combined loading.

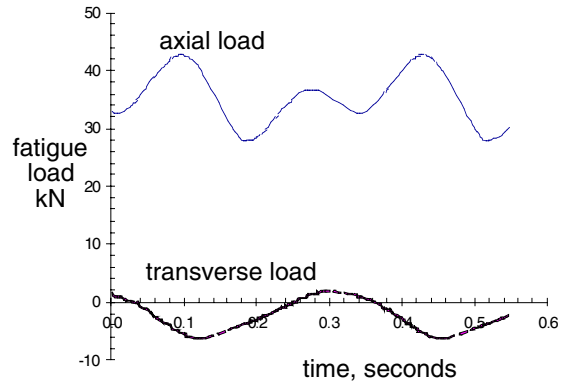
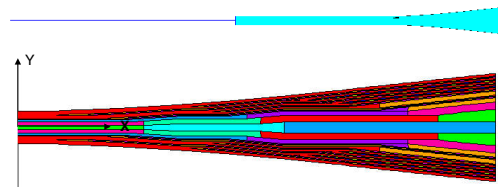


Figure 6. Typical load-time history of GLMS specimen under axial tension and cyclic bending fatigue loading.



Note: Not to scale

Figure 7. Finite element model of GLMS specimen: full model (above) and taper region showing discrete materials by color.

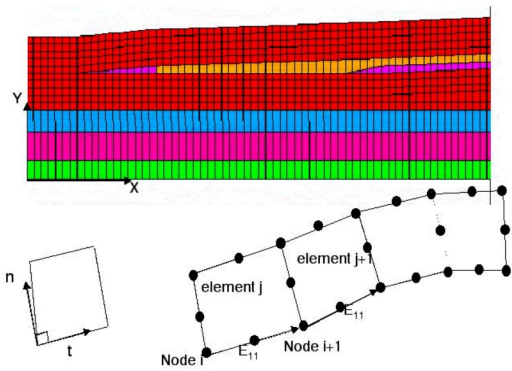


Figure 8. Close-up of finite element model at ply-ending 111 and local element orientation.

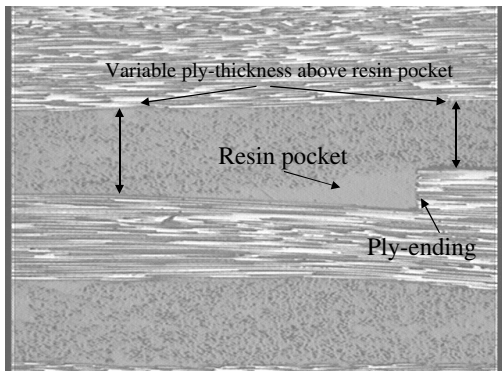
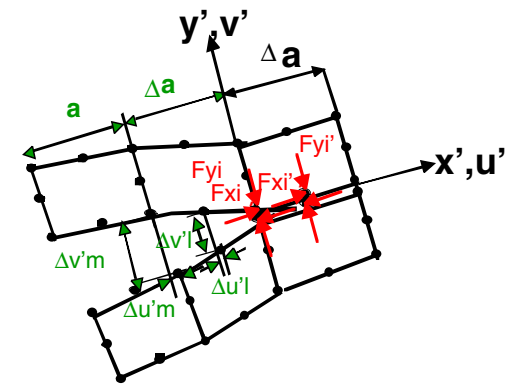


Figure 9. Photomicrograph of ply-drop region with resin pocket and ply-ending.



$$G_I = \frac{1}{2\Delta a} (F'_{yi} \Delta v'_m + F'_{yj} \Delta v'_l)$$

$$G_{II} = \frac{1}{2\Delta a} (F'_{xi} \Delta u'_m + F'_{xj} \Delta u'_l)$$

$$G_T = G_I + G_{II}$$

Figure 10. Virtual Crack Closure Technique (VCCT) loads and displacements in local coordinate system [21].

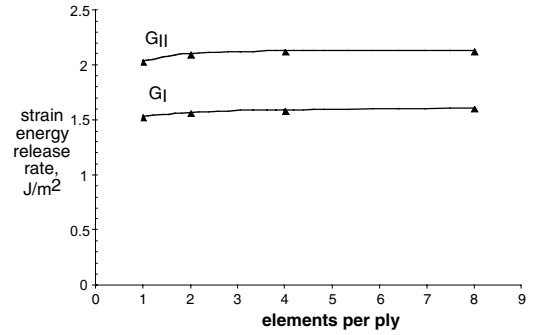


Figure 11. Effect of mesh size on strain energy release rate in tapered flexbeam FE model.

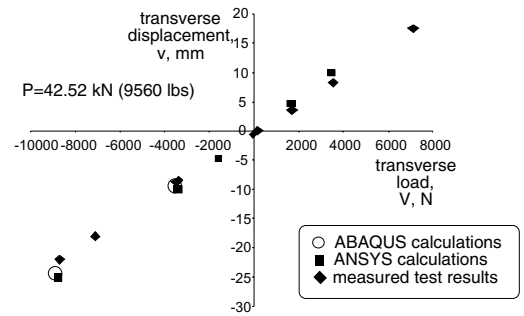


Figure 12. Measured and ANSYS and ABAQUS calculated transverse displacement for GRMS tapered flexbeam with constant axial tension load.

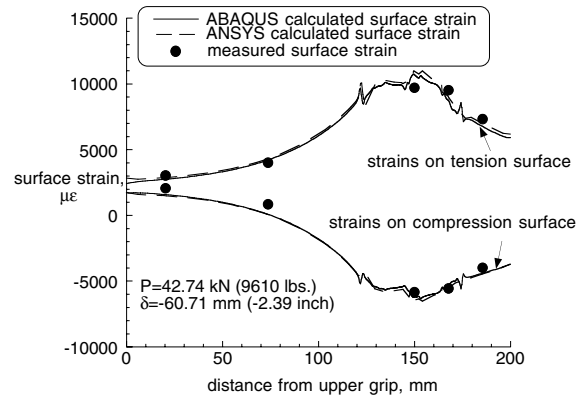


Figure 13. Measured and calculated surface strains in GRMS tapered hybrid flexbeam.

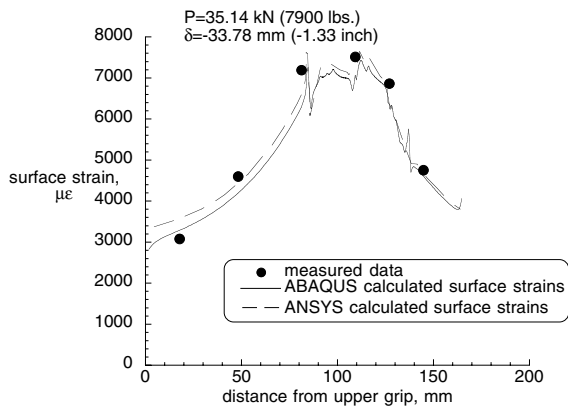
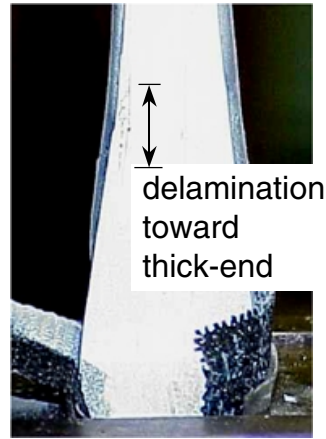
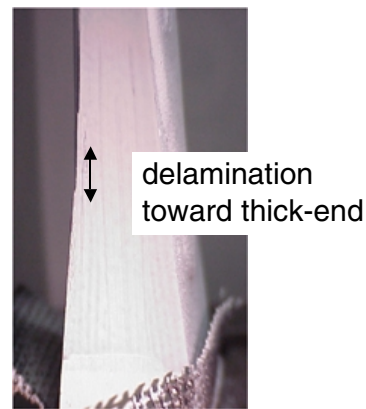


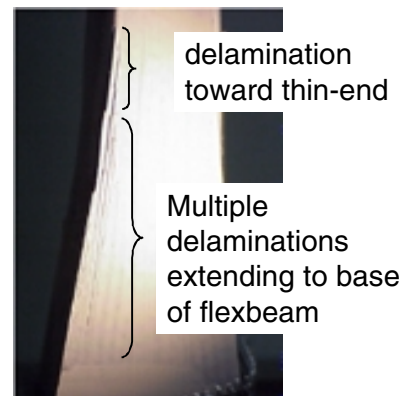
Figure 14. Measured and calculated surface strains in GLMS tapered hybrid flexbeam.



(a) N=49,000 cycles



(b) N=55,880 cycles



(c) N=119,300 cycles

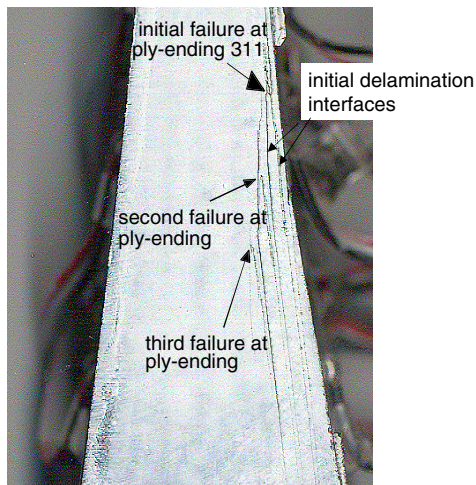


Figure 15. Delamination damage in GRMS flexbeam specimen with N=43,900 cycles.

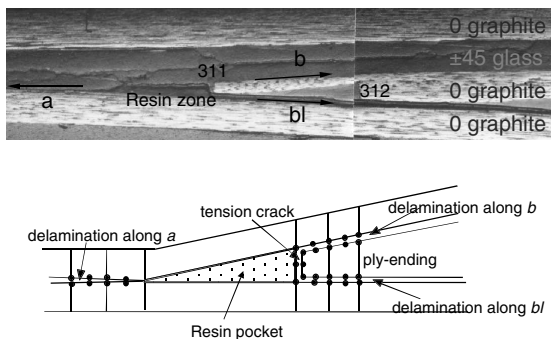


Figure 16. Photomicrograph of 311 ply-drop region of GRMS specimen after 43,900 fatigue cycles and schematic of FE modeling at ply-ending.

Figure 17 (a), (b), (c). Delamination growth on back edge of GLMS1 hybrid flexbeam under fatigue tension-bending loading.

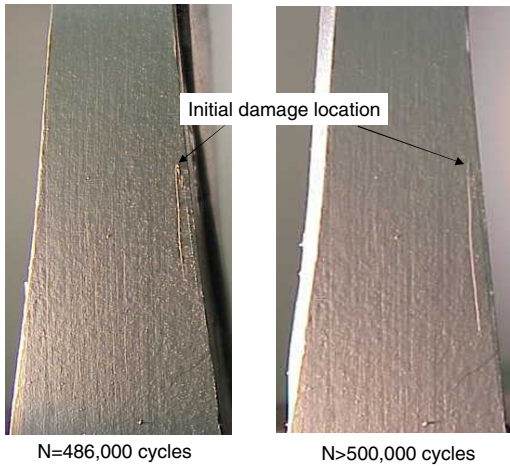


Figure 18. Delamination growth on front edge of GLMS2 flexbeam.

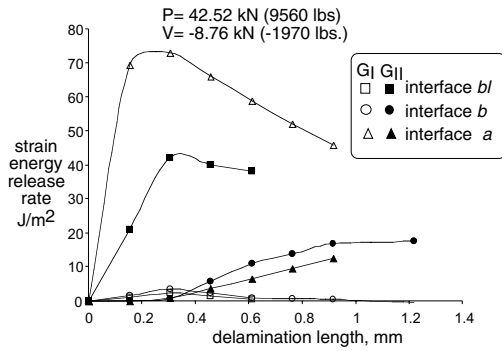


Figure 19. ANSYS calculated strain energy release rates along *a*, *b*, and *bl* paths at ply-ending 111 for GRMS specimen.

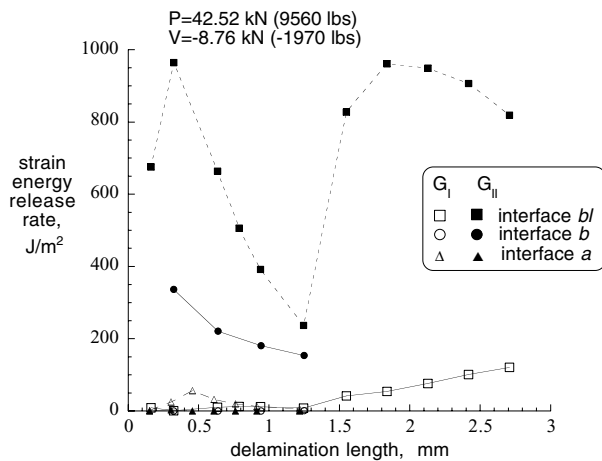


Figure 20. ANSYS calculated strain energy release rates along *a*, *b*, and *bl* paths at ply-ending 311 for GRMS specimen.

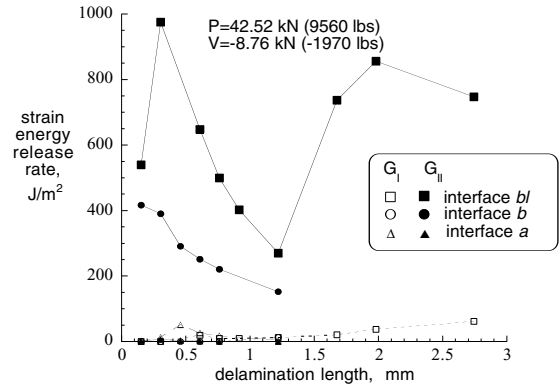


Figure 21. ABAQUS calculated strain energy release rates along *a*, *b*, and *bl* paths at ply-ending 311 for GRMS specimen.

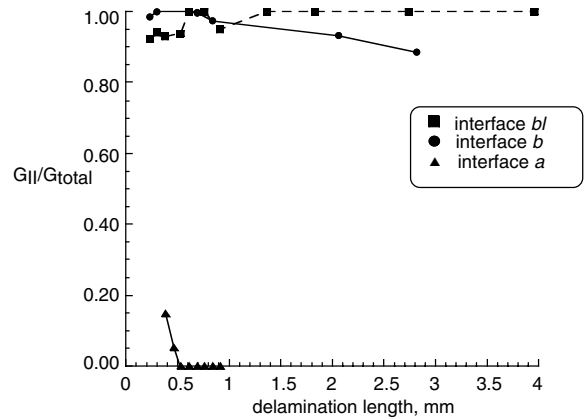


Figure 22. ABAQUS calculated percentage of mode II for delamination along *a*, *b*, and *bl*, at ply-ending 311, in GRMS specimen.

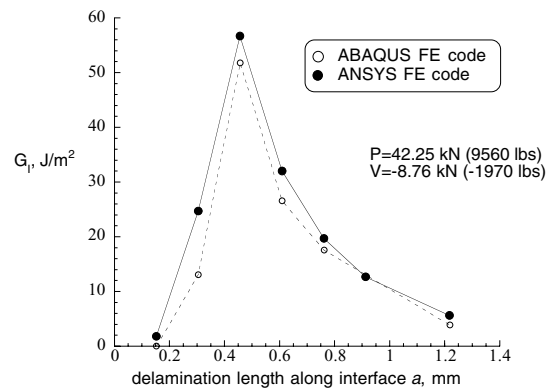


Figure 23. Comparison of  $G_I$  calculations from ANSYS and ABAQUS for delamination along interface *a* at ply-ending 311.

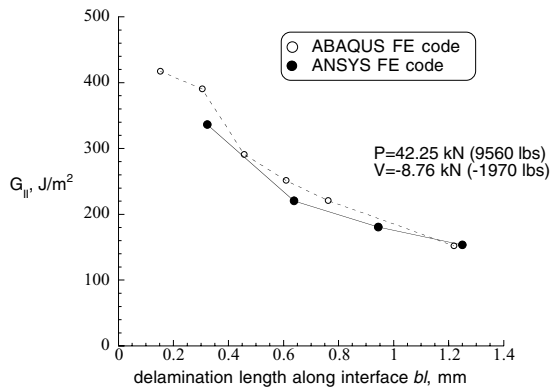


Figure 24. Comparison of  $G_{II}$  calculations from ANSYS and ABAQUS for delamination along interface  $b$  at ply-ending 311.

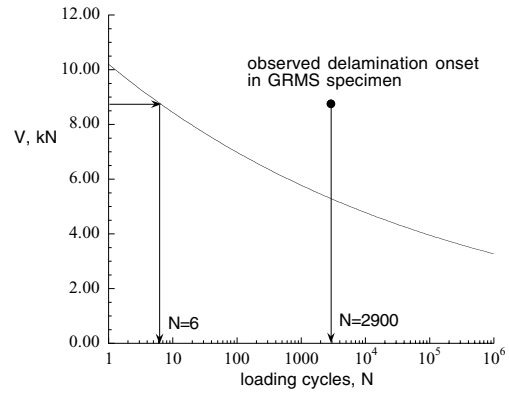


Figure 27. Fatigue life vs. transverse bending load for tapered hybrid flexbeam laminate with constant axial tension load.

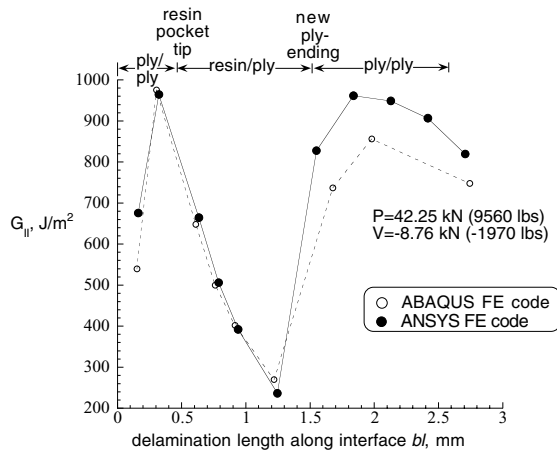


Figure 25. Comparison of  $G_{II}$  calculations from ANSYS and ABAQUS for delamination along interface  $b_l$  at ply-ending 311.

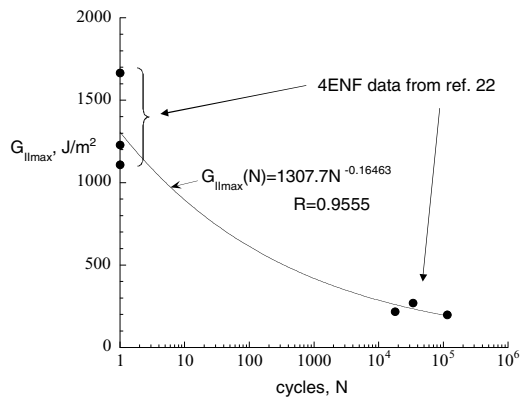


Figure 26. Delamination onset data and fitted curve for cyclic mode II 4ENF tests of graphite/epoxy.